Postprint of: Jiang C., Masrurotin M., Ramezani M., Wibisono A. T., Toyserkani E., Macek W., Sintering Parameter Investigation for Bimetallic Stainless Steel 316L/Inconel 718 Composite Printed by Dual-Nozzle Fused Deposition Modeling, RAPID PROTOTYPING JOURNAL (2024), DOI: 10.1108/RPJ-04-2024-0163

Sintering parameter investigation for bimetallic stainless steel 316L/inconel 718 composite printed by dual-nozzle fused deposition modeling

AQ:1
AQ:2

Cho-Pei Jiang
Department of Mechanical Engineering, National Taipei University of Technology, Taipei, Taiwan and
Additive Manufacturing Center for Mass Customization Production, National Taipei University of Technology, Taipei, Taiwan

Masrurotin Masrurotin
Department of, National Taipei University of Technology, Taipei, Taiwan

Maziar Ramezani
Department of Mechanical Engineering, Auckland University of Technology, Auckland, New Zealand

Alvian Toto Wibisono
Department of Materials and Metallurgical Engineering, Institut Teknologi Sepuluh Nopember, Surabaya, Indonesia

Ehsan Toyserkani
Department of Mechanical and Mechatronics Engineering, University of Waterloo, Waterloo, Canada, and

Wojciech Macek
Faculty of Mechanical Engineering and Ship Technology, Gdansk University of Technology, Gdansk, Poland

Abstract

AQ: 3 **Purpose** – Fused deposition modeling (FDM) nowadays offers promising future applications for fabricating not only thermoplastic-based polymers
AQ: 4 but also composite PLA/Metal alloy materials, this capability bridges the need for metallic components in complex manufacturing processes. The research is to explore the manufacturability of multi-metal parts by printing green bodies of PLA/multi-metal objects, carrying these objects to the
AQ: 5 debinding process and varying the sintering parameters.

Design/methodology/approach – Three different sample types of SS316L part, Inconel 718 part and bimetallic composite of SS316L/IN718 were effectively printed. After the debinding process, the printed parts (green bodies), were isothermally sintered in non-vacuum chamber to investigate the fusion behavior at four different temperatures in the range of 1270 °C–1530 °C for 12 h and slowly cooled in the furnace. All samples was assessed including geometrical assessment to measure the shrinkage, characterization (XRD) to identify the crystallinity of the compound and microstructural evolution (Optical microscopy and SEM) to explore the porosity and morphology on the surface. The hardness of each sample types was measured and compared. The sintering parameter was optimized according to the microstructural evaluation on the interface of SS316L/IN718 composite.

Findings – The investigation indicated that the de-binding of all the samples was effectively succeeded through less weight until 16% when the PLA of green bodies was successfully evaporated. The morphology result shows evidence of an effective sintering process to have the grain boundaries in all samples, while multi-metal parts clearly displayed the interface. Furthermore, the result of XRD shows the tendency of lower crystallinity in SS316L parts, whilst IN718 has a high crystallinity. The optimal sintering temperature for SS316L/IN718 parts is 1500 °C. The hardness test concludes that the higher sintering temperature gives a higher hardness result.

Originality/value – This study highlights the successful sintering of a bimetallic stainless steel 316 L/Inconel 718 composite, fabricated via dual-nozzle fused deposition modeling, in a non-vacuum environment at 1500 °C. The resulting material displayed maximum hardness values of 872 HV for SS316L and 755.5 HV for IN718, with both materials exhibiting excellent fusion without any cracks.

Keywords Bimetallic composite, Fused deposition modeling, Stainless steel 316L, Inconel 718, Sintering

Paper type Research paper

The current issue and full text archive of this journal is available on Emerald Insight at: **https://www.emerald.com/insight/1355-2546.htm**

Rapid Prototyping Journal

[DOI 10.1108/RPJ-04-2024-0163]

The authors would like to thank the High-Value Biomaterials Research and Commercialization Center of NTUT in the Higher Education Sprout Project framework of the Taiwan Ministry of Education (MOE).

Received 11 April 2024
Revised 13 June 2024
Accepted 27 June 2024

J_ID: RPJ ART NO: 10.1108/RPJ-04-2024-0163 Date: 13-July-24 Page: 2 Total Pages: 15 4/Color Figure(s) ARTTYPE="ResearchArticle"

1. Introduction

Additive Manufacturing (AM), commonly known as 3D printing, is a revolutionary technique for fabricating three-dimensional objects through the layer-by-layer deposition of material. Originating in the 1980s (Abdulhameed *et al.*, 2019; Thompson *et al.*, 2019), AM has gained significant traction in recent years, driven by advancements in materials science and processing capabilities. The innovative nature of AM distinguishes it from conventional production methods, eliminating the need for multiple steps such as assembling, machining, milling or other traditional techniques (Caminero *et al.*, 2021). Instead, AM relies on computer-aided design (CAD) software to conceptualize products, followed by processing in specialized AM software to convert the digital design into a printable file. The final step involves constructing the object layer by layer through the 3D printing process. Another convenience using AM beyond traditional manufacturing processes are including as increased design freedom, less material waste and shorter production timelines for low-volume or bespoke items. Those advantage grow the market demand on producing component in the various material such as polymer, ceramic and especially metals. There are some common AM technologies that are used to creating metal parts among selective laser melting (SLM), powder bed fusion (PBF), electron beam melting (EBM), direct energy deposition (DED). All these techniques utilize either beam or laser which expand high-energy source which results in considerable power usage. Moreover, there are big expenditure to maintain the machine and processing unprocessed powder or other feedstock materials.

Recent research has witnessed a surge in investigations focused on fabricating metal parts using material extrusion techniques, particularly fused deposition modeling (FDM). FDM has gained popularity due to its economic production capabilities and reduced power consumption. Notably, it has emerged as an alternative method for producing metal parts, with recent advancements in materials involving the innovation of filament composition by incorporating ceramic or metal powder mixed with polymer. This metal-filled polymer is then extruded through an FDM nozzle, and post-processing steps, including de-binding and sintering processes are employed to achieve the final product (Caminero *et al.*, 2021; Kan *et al.*, 2021; Boschetto *et al.*, 2022; You *et al.*, 2023).

A notable development in FDM involves the combination of high-concentration metal powders with a thermoplastic binder, such as PLA/SS316L (Kurose *et al.*, 2020; Liu *et al.*, 2020; Jiang and Ning, 2021; You *et al.*, 2023), PLA/high carbon (Mousapour *et al.*, 2021) and PLA/bronze (Wei *et al.*, 2022). These combinations allow for the melting and extrusion of materials through the printer nozzle during the FDM process. Presently, the most frequently utilized materials in additive manufacturing include 316 L stainless steel and Inconel 718 nickel superalloy (Maksimkin *et al.*, 2022). This article aimed to contribute to the expanding body of knowledge on additive manufacturing, specifically focusing on the advancements in metal fabrication techniques using FDM and novel material combinations.

Bimetallic materials, characterized by the amalgamation of two distinct metals or alloys, have found widespread utility across diverse applications, including the fields of automobile, aerospace, energy and nuclear industries (Singh *et al.*, 2021; Yang *et al.*, 2022; Mahmud *et al.*, 2023). Notably, their deployment in the automotive sector has been a subject of considerable investigation, with studies focused on weight reduction in components such as body frames, engine blocks and pistons (Bandyopadhyay *et al.*, 2022). Stainless Steel (SS) 316 L stands out as a favored material alloy, owing to its multifaceted advantages encompassing high corrosion resistance, elevated temperature tolerance, robust strength, durability and cost-effectiveness (Pang *et al.*, 2019). In parallel, Inconel 718 (abbreviated as IN718), a nickel-based superalloy, is renowned for its exceptional attributes, including high strength, corrosion resistance and resistance to elevated temperatures (Li *et al.*, 2020). The synergistic combination of IN718 and SS316L offers substantial benefits, notably enhanced corrosion resistance. Both materials exhibit high resistance to corrosion, rendering the composite suitable for applications in challenging and corrosive environments (Jiang *et al.*, 2022). Furthermore, the amalgamation of these two materials imparts the resulting joint with the capability to withstand extreme temperatures, broadening its scope of applicability in demanding operational conditions such as what is reported on ALSTOM Power Sweden that these combination metals are used to create the compressor rotor in which the high-pressure compressor stages are built of Inconel 718[5,6]. The low compressor stage is fabricated from austenitic-based stainless steel. Another application of these dissimilar metals was used as 3161 flexible hoses connected to a heat exchanger with the quick disconnects (QD) made from Inconel 718, in which both materials were butt-joint welded[7]. AQ: 6

This study contributes to the exploration of bimetallic materials, specifically focusing on the advantageous properties arising from the combination of IN 718 and SS316L. The enhanced corrosion resistance and temperature tolerance of this bimetallic composition hold promise for applications in severe environmental conditions, emphasizing the potential impact of such materials in critical industries.

Limited research has been conducted on the utilization of FDM technology for the fabrication of metal parts incorporating metal powder-filled polymer filaments, followed by subsequent de-binding and sintering treatments. In a study by Xinfen Kan *et al.* (2021), fused filament fabrication (FFF) was employed to create SS316L green parts and optimal results were achieved by varying the de-binding temperature to attain high density. Another study conducted by Miguel *et al.* (Caminero *et al.*, 2021) utilized the FFF method to manufacture SS316L metal parts, employing degreasing and sintering processes. Their investigation aimed to enhance mechanical properties by altering angular construction directions. Notably, there is a dearth of literature on the dual-metal printing of SS316/IN718 to the best of the authors' knowledge, highlighting a significant research gap in this area. This study addresses this gap by presenting novel insights into the dual-metal printing process, specifically focusing on SS316/Inconel718, contributing to the expanding knowledge base in the realm of additive manufacturing technologies for metal parts.

This study aims to comprehensively investigate bimetallic 3D printing utilizing SS316L/IN718 through a dual-nozzle

J_ID: RPJ ART NO: 10.1108/RPJ-04-2024-0163 Date: 13-July-24 Page: 3 Total Pages: 15 4/Color Figure(s) ARTTYPE="ResearchArticle"

FDM approach. The research endeavors to offer detailed insights spanning from the initial printed part to the subsequent sintered components. The assessment encompasses the examination of compositional distribution, microstructural evolution, phase transformation and hardness properties that manifest during the sintering process at various temperatures under ambient environmental conditions. The study seeks to contribute valuable information to the understanding of the intricacies involved in the bimetallic 3D printing of SS316L/IN718, providing a nuanced exploration of the material characteristics and properties throughout the fabrication and sintering stages.

2. Materials and experimental methods

2.1 Materials

This study employed metallic filaments composed of stainless steel 316 L and IN718 (The Virtual Foundry Co., USA). Both filaments incorporate PLA as the binder, which encompasses a high metal content. The stainless steel 316 L filament, when combined, yielded a density of 3.5 g/cm^3, with an approximate metal weight percentage of 87 Wt.%. Conversely, the Inconel 718 filament exhibited a density of 3.98 g/cm^3 and contained around 84 Wt.% of metal. The individual metal densities of SS316L and IN718 are reported as 8.00 g/cm^3 (Yakout *et al.*, 2018; Jiang *et al.*, 2021; Jiang *et al.*, 2022) and 8.22 g/cm^3 (Balbaa *et al.*, 2020), respectively. Figure 1 presents a comprehensive overview of the morphology, particle size distribution and metallic composition of both metal-filled filaments. The particle size analysis presents that the grain sizes of SS316L and IN718 are in range of 12–52 and 10–50 μm respectively, revealing that both have comparable grain size. Additionally, Table 1 presents the average spherical metallic powder characteristics within the filaments, indicating that the grain size of SS316L is slightly larger than that of IN718. This meticulous characterization provides crucial insights into the materials employed in the study, laying the foundation for a comprehensive analysis of their behavior in the subsequent 3D printing and sintering processes.

2.2 Printing parameter and benchmark

The fabrication of green parts was conducted using a dual-extruder 3D printer manufactured by Humble Technology Co., Taiwan. The printer's two extruders are equipped with 0.4 mm-diameter nozzles. A detailed overview of the print parameters is provided in Table 2, indicating specific values for initial layer height, layer thickness, line width and wall thickness (0.2, 0.3, 0.4 and 0.8 mm, respectively). In consideration the metal powder, the experimental trials was conducted to obtain smooth surface finish in printing results. The plate temperature was maintained at 70°C, and the printing speed for both nozzles was set at 40 mm/s. Notably, distinct printing temperatures were applied; 190°C for the IN718 filament and a higher temperature of 200°C for the SS316L filament. The research adopted parameters tailored for metal-filled filaments, necessitating adjustments for the IN718 and SS316L printing parameters, along with the heat configuration of the build platform. The build printing orientation was flat.

As it is illustrated in Figure 2, the distribution of metal fill within a layer, facilitated by the binder, has quite homogeneous and well-dispersed metal distribution. The homogeneous distribution of metal in the metallic filament printing layers is a pivotal determinant of the final product's quality and integrity. This meticulous attention to the printing parameters and metal distribution is essential for ensuring the overall success of the 3D printing process and subsequent sintering stages.

This study introduces three distinct benchmark types, each possessing dimensions of 12 mm (length) × 8 mm (width) × 3.2 mm (height), as depicted in Figure 3. The butt-joint configuration is used for bimetallic design for ease fabrication and interface measurement. To ensure the reliability of the measured data, a total of 12 specimens for each benchmark were systematically printed and replicated. This meticulous approach to producing multiple specimens enhances the robustness of subsequent experiments and strengthens the validity of the obtained data.

2.3 Shrinkage and density measurement

Volume, weight and density measurements were conducted on samples from the printing, debinding and sintering processes, utilizing digital scales and gauge callipers. The porosity percentages were obtained by capturing the polished surface of parts using an optical microscope (Whited MW 100, Huaide Industrial. Co. Ltd., Taiwan) in three times of each parts in the fixed magnification. These captured images were examined and analyzed by (Image J version 1.52n, NIH and LOCI, USA). Based on the distinct separation of the bright and dark patches, the software computed the porosity and solid area. The density ratios were determined employing the method developed by Shi *et al.* (2020). The calculated density values, denoted as ρ_{cal} (g/cm^3), were obtained by multiplying the relative density by the respective theoretical bulk density values of SS316L (8.00 g/cm^3) and IN718 (8.22 g/cm^3) as proposed by Shi *et al.* (2020) and Jiang *et al.* (2022). The density values were determined using equations (1)–(2), outlined as follows:

$$\rho_{cal} = \rho_{cal-rel} \times \rho_{theory} \tag{1}$$

$$\rho_{cal-rel} = \left(1 - \frac{A_{lack}}{A_{total}}\right) \times 100\% \tag{2}$$

where A_{lack} denotes the amount of porosity area, A_{total} equals the total area of micrograph figure and $\rho_{cal-rel}$ (%) denotes the computed relative density. The solid area was determined using the relative equation based on the obtained micrographs.

2.4 Thermal analysis for debinding

Thermogravimetric analysis (TGA) conducted with the HITACHI STA7300 instrument from Hitachi Corp., Japan, was employed to determine the optimal temperature for the debinding of binders in both filaments. This analysis was performed under an air atmosphere. The two metallic filaments underwent heating to 900°C in a nitrogen atmosphere, and the recorded degradation of material mass was indicative of the binder removal process.

2.5 Sintering and post-processing

Following the FDM process, the essential steps in manufacturing metal parts encompassed the subsequent de-binding and

J_ID: RPJ ART NO: 10.1108/RPJ-04-2024-0163 Date: 13-July-24 Page: 4 Total Pages: 15 4/Color Figure(s) ARTTYPE="ResearchArticle"

Figure 1 Metallic filament characterizations provides SEM images cross-sections, metal grain size distribution and element composition in the metallic filaments (include metal powders and its binder)

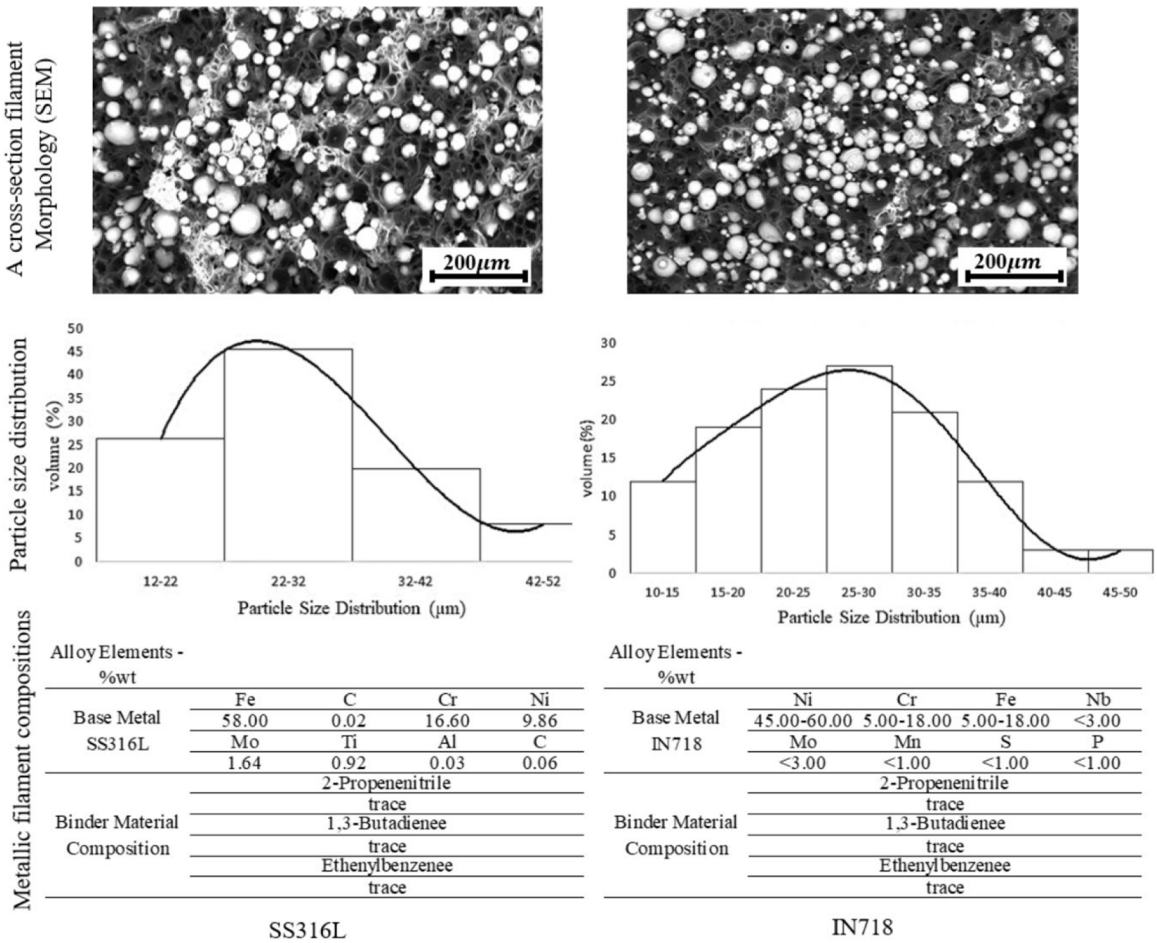

Source: Author's own work

Table 1 The grain size average of metallic filament in percentile

Percentile rank	SS316L	Inconel 718
d = 10	17,661	14,898
d = 50	27,997	26,469
d = 90	39,452	38,108

Source: Authors' own work

sintering phases, achieved through a thermal process. A furnace (Carbolite Gero 30°–3000°) was employed for debinding and sintering, involving gradual heating, controlled dwell periods and a gradual cooling phase without opening the furnace. The thermal debinding temperature for each benchmark was determined based on the outcomes of thermogravimetric analysis (TGA). The debinding process is initiated by heating the green part to eliminate the binder, resulting in what is commonly referred to as the "brown part." Subsequently, the brown parts underwent controlled heating at 1360°C for SS316L, 1530°C for IN718 and 1500°C for the bimetallic part. This systematic approach ensured the successful removal of the binder and sintering of the metal parts, contributing to the overall quality of the fabricated components.

Post-processing procedures, including metallographic preparation, were meticulously executed to achieve high-resolution optical microscope images. Initially, the process involved mounting

Table 2 The distinct parameters setting for printing parts in SS316L and IN718 metallic filaments

Parameter	Initial layer height	Layer thickness	Line width	Wall thickness	The temperature of printing	Build plate temperature	Top/bottom pattern	Print speed
Value	0.2	0.3	0.4	0.8	190 and 200	70	Concentric	40
Unit	mm	mm	mm	mm	°C	°C	–	mm/s

Source: Authors' own work

J_ID: RPJ ART NO: 10.1108/RPJ-04-2024-0163 Date: 13-July-24 Page: 5 Total Pages: 15 4/Color Figure(s) ARTTYPE="ResearchArticle"

Figure 2 The distribution of metal powder in printing results in the surface layers

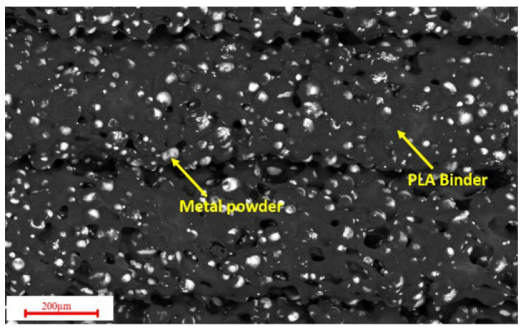

Source: Author's Own work

all samples to provide structural support and facilitate ease of handling during polishing. The samples were embedded in a mounting material comprising a mixture of epoxy resin and its hardener (polyoxypropylene diamine) in a precise ratio of 3:2. Once mounted, the samples underwent a polishing regimen utilizing standard alumina grinding discs with progressively finer grits: P200, P320, P600, P800 and P1200. This method ensured the attainment of well-prepared samples for subsequent high-quality optical microscope imaging.

2.6 Microstructural and mechanical characterization

The identification of polymeric constituents in the filaments was conducted through Fourier Transform Infrared (FTIR) testing. The commercial metallic filaments, comprising various elements, underwent analysis for surface morphology, chemical compositions and phase transformations using Scanning Electron Microscopy with Energy Dispersive X-ray Spectroscopy (SEM-EDX) and X-ray Diffraction (XRD) as analytical tools. An Energy Dispersive X-ray Analyzer (EDX), specifically the X-max Oxford Instrument from Oxford, UK, was utilized to assess the chemical compounds of FDMed and post-processing parts, respectively. For the identification of phases in both the as-received SS316L powder and the fabricated specimens, representative samples were subjected to examination using an X-ray diffraction (XRD) spectrometer (Bruker D2Phaser, Karlsdorf, Germany) with Cu-K radiation in the range of 2theta from 30 to 130. The Vickers Hardness tester by Shimadzu Co. Ltd., Tokyo, Japan, developed the Vickers Hardness test (HV0.5 scale) in accordance with the American Society for Testing and Materials (ASTM) E92-82 standards. The completed various tests on metallic parts are depicted in Figure 4 which shows the workflow of measurement of microstructure, characterization and hardness properties. This comprehensive approach ensures a thorough assessment of the materials' composition, structural characteristics and mechanical properties in the printed and sintered metal parts.

3. Results and discussion

3.1 Result of thermogravimetric analysis

Thermal analysis was conducted to determine the optimal temperature for evaporating the binder from the metal powders. Following the manufacturer's guidelines, the printing object underwent heating at 204°C for 2 h, with a subsequent gradual increase to 408°C, where it was maintained for 3 h (Wei *et al.*, 2022). Figure 5 illustrates distinct outcomes for the thermal decomposition of the two metal-filled filaments' binders. The testing of SS316L and IN718 metal-filled filaments was carried out under nitrogen atmosphere, ranging from ambient temperature to 1000°C. The complete removal of the binder was observed at temperatures exceeding approximately 500°C. The degradation of the SS316L filament's binder commenced around 320°C, whereas the IN718 counterpart initiated degradation at approximately 360°C, preceding any melting. The weight loss percentage for SS316L reached approximately 87%, whereas the weight loss percentage for IN718 was 84%. This thermal analysis provides crucial insights into the temperature profile required for efficient binder removal in the FDMed parts. Therefore, Table 3 presents the sintering temperature for each benchmark.

The debinding process initiated by heating the green part to a temperature of 204°C for 2 h, followed by a gradual increase to 408°C, where it was held for an additional 3 h to facilitate the removal of the binder. This phase resulted in what is commonly referred to as the "brown part." Subsequently, the brown parts of SS316L, IN718 and the bimetallic variant underwent a controlled heating process to achieve sintering, involving four gradual steps as outlined in Table 3. The heating temperatures were set at 1360°C, 1530°C and 1500°C for SS316L, IN718 and the bimetallic type, respectively. This systematic approach ensured the effective removal of the binder during de-binding and facilitated the subsequent sintering process for the desired metallic components.

3.2 FDMed samples and dimensional measurement

Figure 6 provides a comprehensive visual analysis, highlighting three distinct stages: as-printing (grey color), debinding (brown color) and sintering (silvery-white). The green parts displayed

Figure 3 Benchmark design of (a) bimetallic of SS316L/IN718, (b) SS316L and (c) IN718

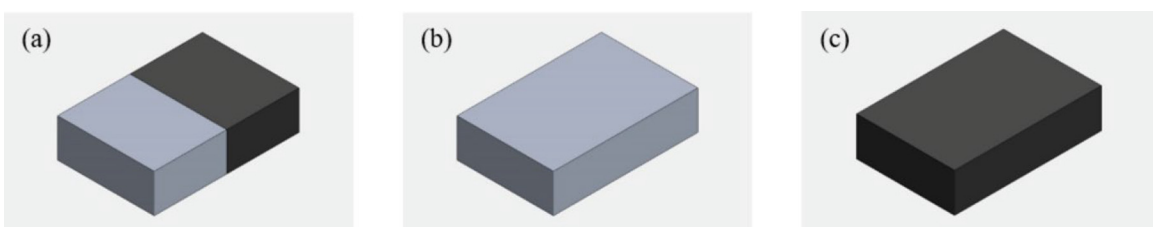

Source: Author's Own work

J_ID: RPJ ART NO: 10.1108/RPJ-04-2024-0163 Date: 13-July-24 Page: 6 Total Pages: 15 4/Color Figure(s) ARTTYPE="ResearchArticle"

Figure 4 The schematic views of the experimental setup of the various tests

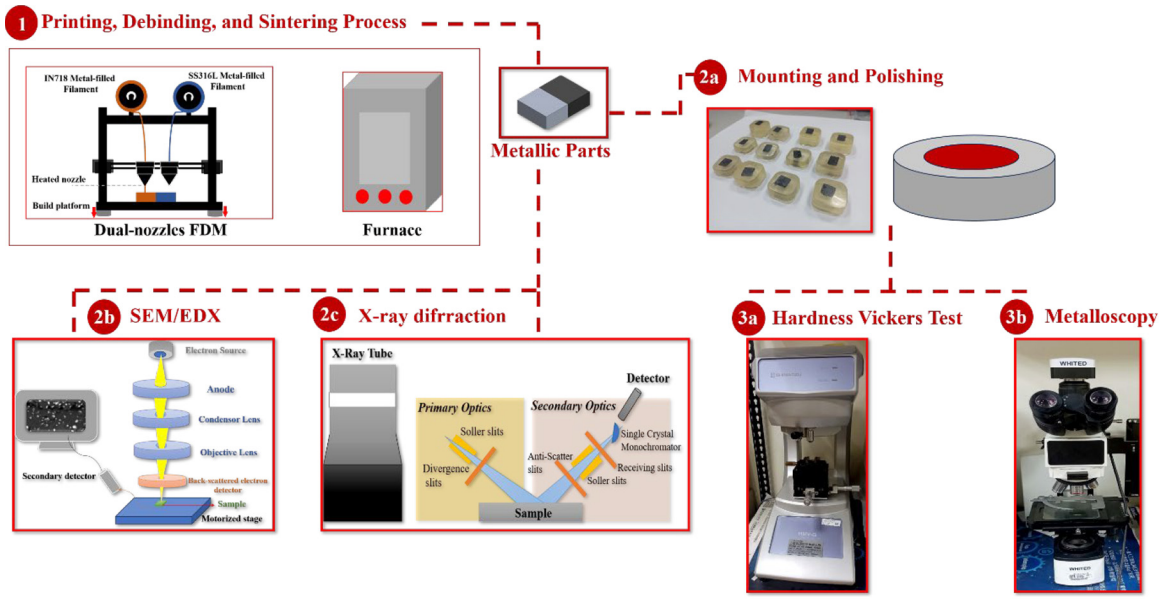

Source: Author's own work

Figure 5 TGA results showing the different weight change percentages of metallic filaments in both SS316L and IN718

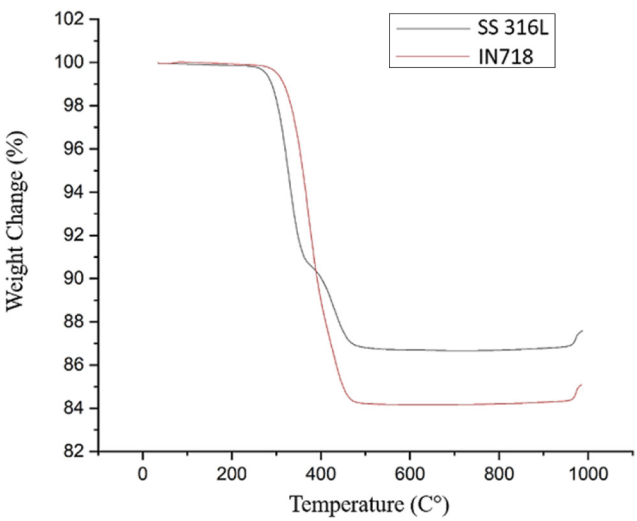

Source: Author's own work

Table 3 Sintering temperature for each type samples

Type	Sintering temperature(°C) 1	2	3	4
SS316L parts	1,270	1,300	1,330	1,360
IN718 parts	1,440	1,470	1,500	1,530
Bimetallic part	1,350	1,400	1,450	1,500

Source: Authors' own work

well-established surface finishes with good layer adhesion. Although the proposed dimensions were $12 \times 8 \times 3.2$ mm, the actual dimensions of all as-printed parts were found to be slightly larger than the design, as detailed in Table 4. Notably, the as-printed IN718 part exhibited larger dimensions compared to SS316L, while the bimetallic part closely approximated the original design dimensions.

Table 4 provides detailed information regarding the x, y and z axes of the printed samples for SS316L, IN718 and SS316L/IN718. Mass measurements were also recorded to assess the precision of the achieved dimensions in comparison to the target values. The data indicates that the average discrepancies between the physical printed samples and their original design models are approximately ± 0.3 mm. These variations can be attributed to hardware settings and slicing software parameters.

Mass measurements revealed a varied trend, with SS316L parts weighing more than the other two metallic materials, while IN718 parts exhibited a lighter weight. Considering the bulk densities of SS316L and IN718 at around 8 g/cm^3 (Jiang *et al.*, 2021; Jiang *et al.*, 2022), this discrepancy suggests a lower quantity of IN718 powder in the filament compared to the amount of SS316L. The observed changes in mass across all parts can be attributed to oxide formation, as indicated by the TGA test results, where temperatures above 900°C exhibited an incline in the weight gain curve. This thorough analysis of dimensions and mass provides valuable insights into the precision, material distribution and characteristics of the printed metal parts.

3.3 Fourier-transform infrared spectroscopy

A deeper exploration to discern the chemical interactions within the metallic filament binder involves the identification of the employed polymer, as illustrated in Figure 7. The characteristic

J_ID: RPJ ART NO: 10.1108/RPJ-04-2024-0163 Date: 13-July-24 Page: 7 Total Pages: 15 4/Color Figure(s) ARTTYPE="ResearchArticle"

Figure 6 The appearance of the samples after printing, debinding and sintering

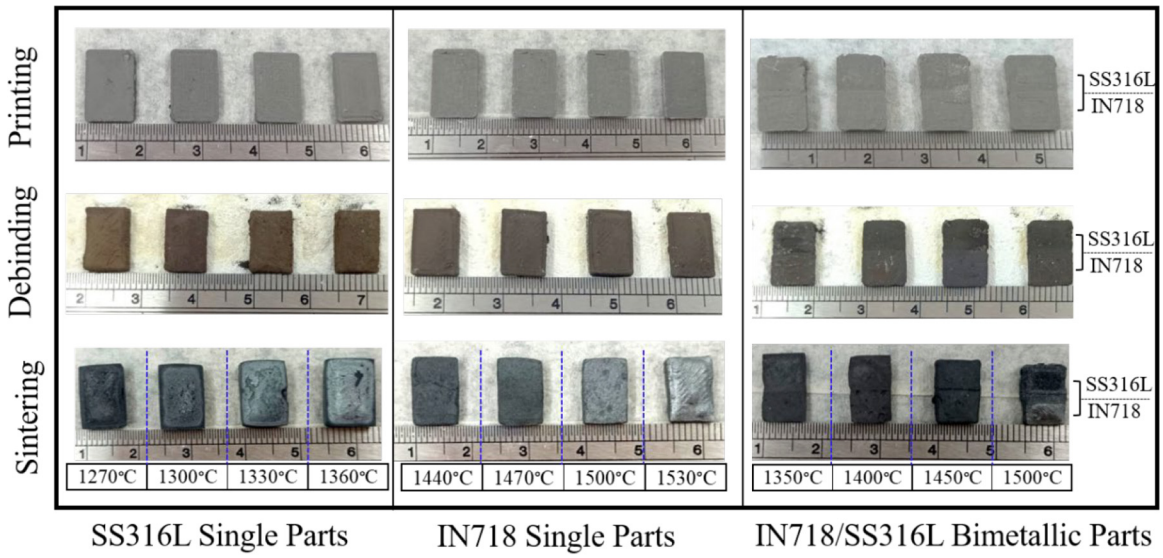

Source: Author's own work

Table 4 The average dimension evolution measurements in the three processing

Samples	Process	Average length (mm)			
		x(width)	*y(length)*	*z(height)*	Mass (g)
SS316L	As-printing	8.17 ± 0.03	12.08 ± 0.02	3.19 ± 0.05	1.47 ± 0.03
	debinding	7.50 ± 0.04	11.38 ± 0.05	3.03 ± 0.15	1.07 ± 0.04
	sintering	8.35 ± 0.11	12.42 ± 0.11	3.43 ± 0.22	1.43 ± 0.08
IN718	As-printing	8.25 ± 0.05	12.24 ± 0.06	3.17 ± 0.03	1.18 ± 0.01
	debinding	7.10 ± 0.01	11.18 ± 0.01	2.77 ± 0.05	0.98 ± 0.01
	sintering	7.89 ± 0.01	11.52 ± 0.04	2.90 ± 0.01	1.18 ± 0.01
SS316L/IN718	As-printing	8.10 ± 0.02	12.02 ± 0.01	3.19 ± 0.01	1.40 ± 0.02
	debinding	7.61 ± 0.02	10.45 ± 0.02	2.97 ± 0.01	1.06 ± 0.01
	sintering	7.83 ± 0.09	10.13 ± 0.44	2.97 ± 0.01	1.3 ± 0.05

Source: Authors' own work

peaks of both IN718 and SS316L reveal analogous patterns, featuring peaks at 2915, 1748, 1456, 1180 and 1078, corresponding to —CH_3, —C = O, C — H, C — H, C — O (COOH) functional groups commonly associated with polylactic acid (PLA) (Jongprateep *et al.*, 2022). Comprehensive details regarding the peak information are provided in Table 5. This investigation contributes to a more profound understanding of the chemical composition of the binder, specifically identifying the presence of PLA in the metallic filaments.

3.4 Debinding and composition of sintered parts

Figure 8 depicts the metal particles, which possess various geometry and sizes including fine spherical powder, coarse spherical powder and irregularly shaped powder. In the debinded parts of SS316L and IN718, a minimal amount of porosity was observed. Despite the physical fragility of the parts, they effectively maintained the structural integrity required for shape retention due to the presence of smaller particles adequately filling the spaces between larger powder particles. The Energy Dispersive X-ray Spectroscopy (EDS) spectrum of the debinded SS316L part exhibits multiple peaks corresponding to elements inherent to SS316L, such as Fe, Cr, Mo, Mn, Ni, along with minor additional elements. Furthermore, the presence of Oxygen and Nitrogen in the spectrum suggests that the sintering process occurred in an environment atmosphere containing these elements (O_2 and N_2). This analysis offers valuable insights into the particle characteristics and porosity levels in the debinded parts of SS316L and IN718, contributing to a comprehensive understanding of the material structure.

The dimensional changes at various processing stages for SS316L single parts, IN718 single parts and the bimetallic composite of SS316L and IN718 components are detailed and presented in Table 6. The percentage shrinkage values represent a comparison between the dimensions at each post-processing stage and the initial dimensions of the printed parts. Following the debinding process, a reduction in size across all linear axes was observed after the removal of the binder for all parts, particularly noticeable in the IN718 single parts. Notably, the shrinkage percentages were higher, reaching up to

J_ID: RPJ ART NO: 10.1108/RPJ-04-2024-0163 Date: 13-July-24 Page: 8 Total Pages: 15 4/Color Figure(s) ARTTYPE="ResearchArticle"

Figure 7 FTIR spectra showing different spectrum patterns in both SS316L and IN718

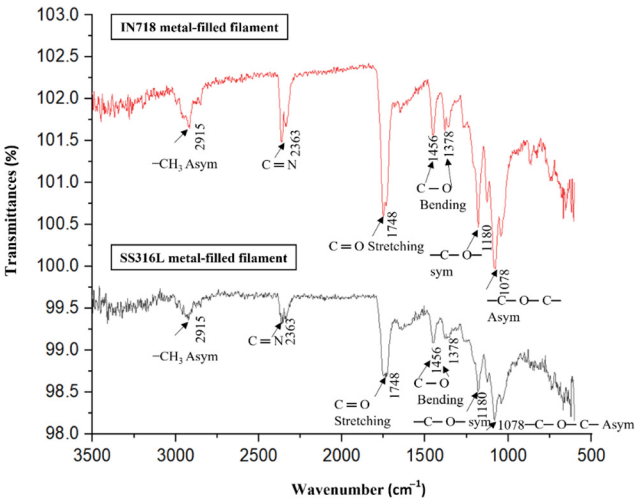

Source: Author's own work

Table 5 FTIR Analysis report presents the peaks of binder in filament

Wavenumber (cm^{-1})	Vibrational mode
2,915	asymmetric–CH3 stretching
1,750	C = O stretching
1,456, 1,378	C–H bending
1,180	C–O symmetric
1,078	—C— O— C— asymmetric

Source: Authors' own work

7.45% in linear *x* and 6.76% in linear *y*. These findings align with the initial measurements, indicating lower density and mass in IN718 green parts, suggesting a lower metal fill in the filament compared to SS316L filaments. Nevertheless, upon subjecting all samples to elevated temperatures, all specimens exhibited an enlargement compared to the previous process. Notably, oxidation occurred, where certain metallic substances reacted with oxygen, resulting in distinct dimensional changes between SS316L parts and other components. Specifically, the results for SS316L demonstrated negative values, indicating an expansion of dimensions after the sintering process compared to the green parts. This phenomenon is attributed to the additional formation of oxide layers. In contrast, the IN718 single parts showed the formation of oxide layers after sintering, evident in the dimension change between debinding and sintering results as detailed in Table 4. For bimetallic parts, a higher shrinkage occurred in linear y during both the debinding and sintering processes. This shrinkage pattern also influenced the results of joining two materials with different thermal behaviors.

3.5 Sintering results

3.5.1 Density and porosity

An optical microscope was performed on sintered deposits of SS316L, IN718 and SS316L/IN718 which were sintered at various temperatures. The images were captured after following some processes namely; the grinding and polishing process to achieve better image resolution. The porosity also accounted for each temperature variable. The supported diagram in Figure 10 represents of the porosity percentages of each part.

Metallographic examinations of the SS316L samples were conducted to scrutinize the impact of sintering temperature on porosity distribution and interfacial bonding, utilizing 20x magnification. With increasing temperature, atoms initiate bonding, forming necks between adjacent particles, leading to a larger solidified area in the SS316L printed part and a reduction in pores. Figure 9(a), captured at a sintering temperature of 1270°C, vividly illustrates numerous small and large pores, totaling approximately 50.44%. Figures 9(b)–(d) showcase denser surface areas compared to lower-temperature sintering. Optimal sintering conditions were observed at 1,360°C, providing the lowest porosity percentage.

In Figure 8(e), the surface observation of IN718 with variable sintering at 1,440°C reveals porosity with both small and larger voids, constituting approximately 61.13%. Subsequently, at a higher variable sintering temperature of 1,470°C [Figure 8(f)], an improvement in densification is observed, leading to a reduced porosity value of 6.62%. Further increasing the variable temperatures to 1,500°C [Figure 9(g)] and 1,530°C [Figure 9(h)] results in a minimal amount of porosity, accounting for 39.30% and 37.16%, respectively. This detailed microstructural analysis offers insights into the porosity variations in IN718 at different sintering temperature.

Figures 9(i)–(l) depict microstructural observations of the SS316/IN718 bimetallic composite sintered part. Figure 9(l) highlights the efficiency of the highest temperature at 1,500°C, yielding reduced porosity in the SS316L/IN718 microstructure. The joint interface of both distinct metals is clearly visible across various sintering temperatures, emphasizing the impact of sintering temperature variation on porosity percentage. At 1,350°C and 1,400°C, IN718 parts exhibit a darker appearance with numerous voids due to a limited number of joined particles. The situation improves slightly at 1,450°C. Notably, at 1,500°C, the IN718 sintered result demonstrates a radical reduction in porosity, reaching 32.57%, indicating that at this temperature and under these conditions, IN718 has begun to approach a state of near-melting. Conversely, SS316L does not exhibit a significant reduction in porosity, suggesting that above 1,330°C, this material initiates the melting process. The determined optimal sintering temperature for SS316L/IN718 parts is 1,500°C. This comprehensive microstructural analysis provides valuable insights into the influence of sintering temperature on the porosity and interface characteristics of the SS316/IN718 bimetallic composite, crucial for optimizing manufacturing processes and material properties.

3.5.2 Microstructural evolution of sintered parts

The post-sintering microstructural evolution is depicted in Figure 11, showing distinct solid bonding behaviors in SS316L, IN718 and bimetallic SS316L/IN718 deposits. At a sintering temperature of 1,270°C for the SS316L part, fine spherical powders exhibit weak contact formation between particles, resulting in well-distributed small pores throughout the part. Clustering of particles occurs, leading to larger grains and neck growth, with the formation of macropores observed at 1,300°C. At higher peak temperatures, grain growth is pronounced,

J_ID: RPJ ART NO: 10.1108/RPJ-04-2024-0163 Date: 13-July-24 Page: 9 Total Pages: 15 4/Color Figure(s) ARTTYPE="ResearchArticle"

Figure 8 SEM and EDS spectrum and chemical composition of the SS316L and IN718 resulting from the removal of the PLA binder

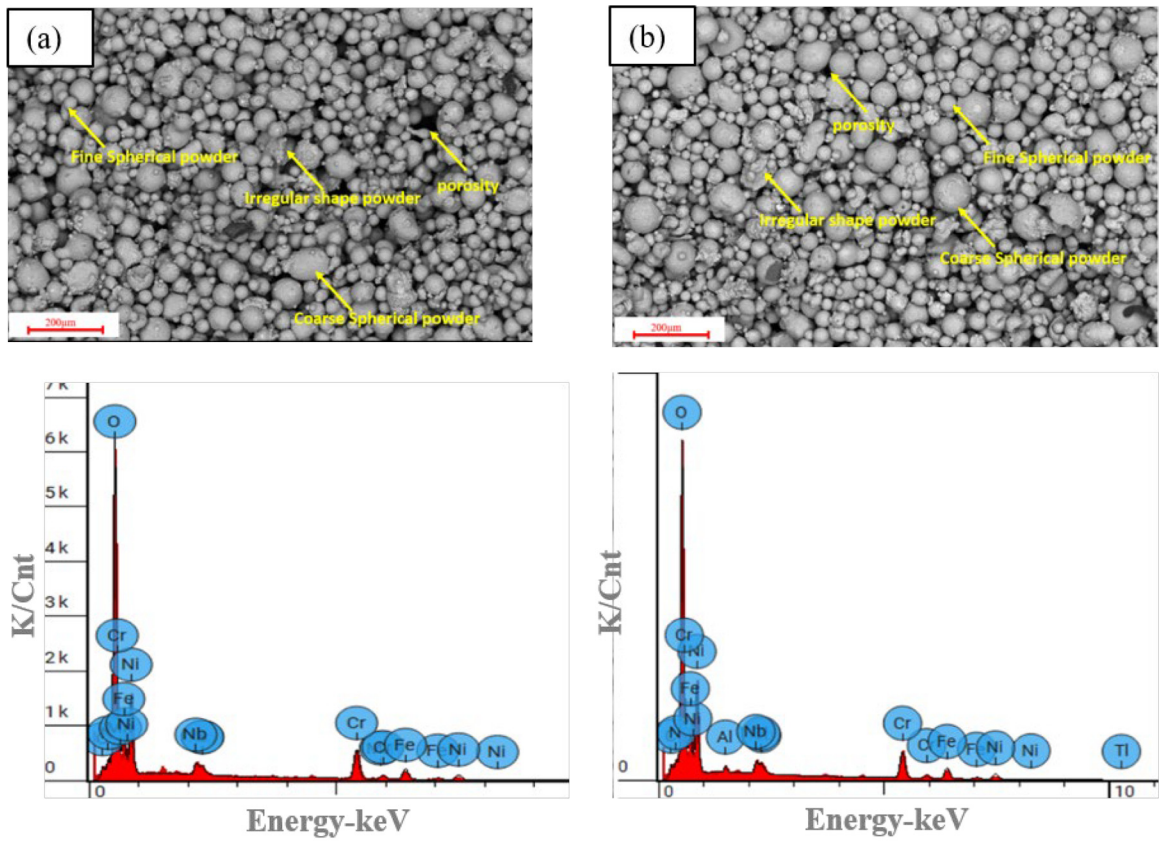

Alloy Elements - %wt

Composition	Fe	C	Cr	Ni	Mo
	24.2	1	23.1	29.8	1.2
	Mn	S	N	O	
	0.4	0.3	2.2	17.8	

Alloy Elements - %wt

Composition	C	N	O	Al	Cr
	1.1	1.6	17	0.6	21
	Fe	Ni	Nb	Mo	Ti
	21	32	3.6	1.4	0.7

Source: Author's own work

Table 6 The observations of percentage shrinkage and density evolution in two post-processing debinding and sintering

Samples	Temperature sintering (°C)	Linier shrinkage *x* (%) (after Debinding)	Linier shrinkage *y* (%) (after Debinding)	Linier shrinkage *z* (%) (after Debinding)	Linier shrinkage *x* (%) (after Sintering)	Linier shrinkage *y* (%) (after Sintering)	Linier shrinkage *z* (%) (after Sintering)	Relative density (%)
SS316L	1,270	4.30 ± 0.15	3.01 ± 0.21	2.57 ± 2.60	−(1.08 ± 074)	-(1.35 ± 045)	-(3.54 ± 3.19)	49.56
	1,300							53.99
	1,330							56.42
	1,360							66.79
IN718	1,440	7.44 ± 0.28	4.49 ± 0.28	6.76 ± 1.23	2.22 ± 0.30	2.99 ± 0.10	4.43 ± 0.60	38.87
	1,470							45.39
	1,500							60.70
	1,530							62.84
SS316L/IN718	1,350	3.13 ± 0.22	7.00 ± 0.18	3.45 ± 0.96	1.68 ± 0.54	8.56 ± 2.15	3.57 ± 0.29	52.19
	1,400							55.36
	1,450							57.62
	1,500							67.24

Source: Authors' own work

J_ID: RPJ ART NO: 10.1108/RPJ-04-2024-0163 Date: 13-July-24 Page: 10 Total Pages: 15 4/Color Figure(s) ARTTYPE="ResearchArticle"

Figure 9 Microstructural observation of sintered parts SS316L, IN718 and bimetallic components SS316L/IN718 at varying temperatures

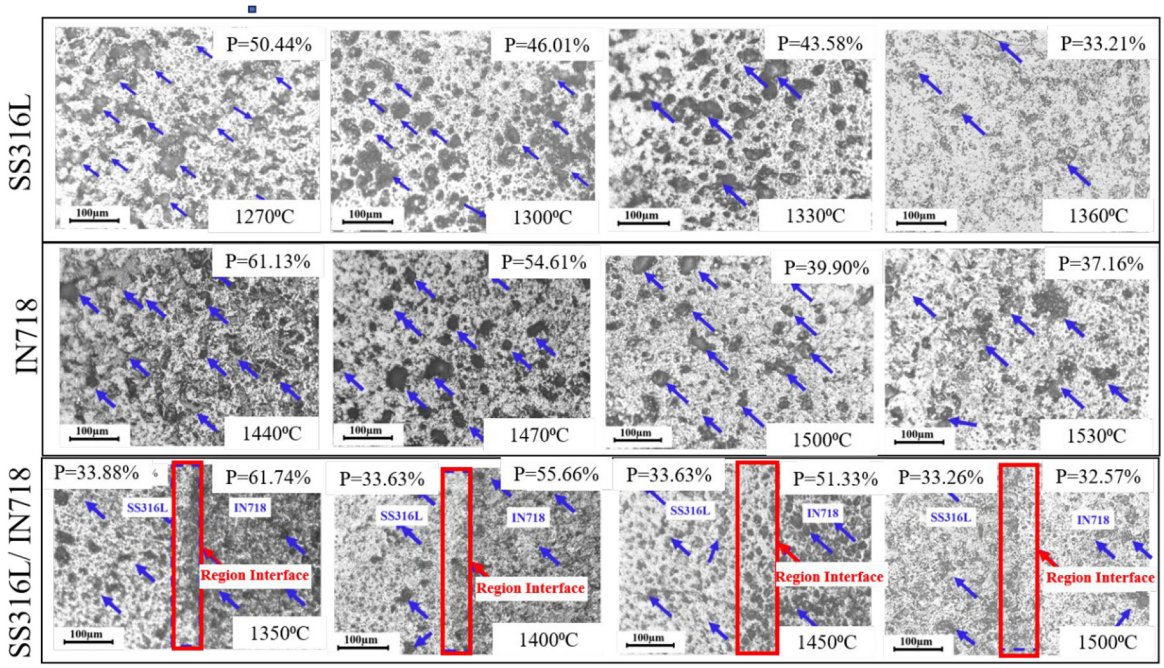

Notes: (*P = porosity,blue arrow show the apparent porosity)
Source: Author's own work

Figure 10 The diagram of porosity percentage for SS316L single part, IN718 single part and Bimetalliic SS316L/IN718

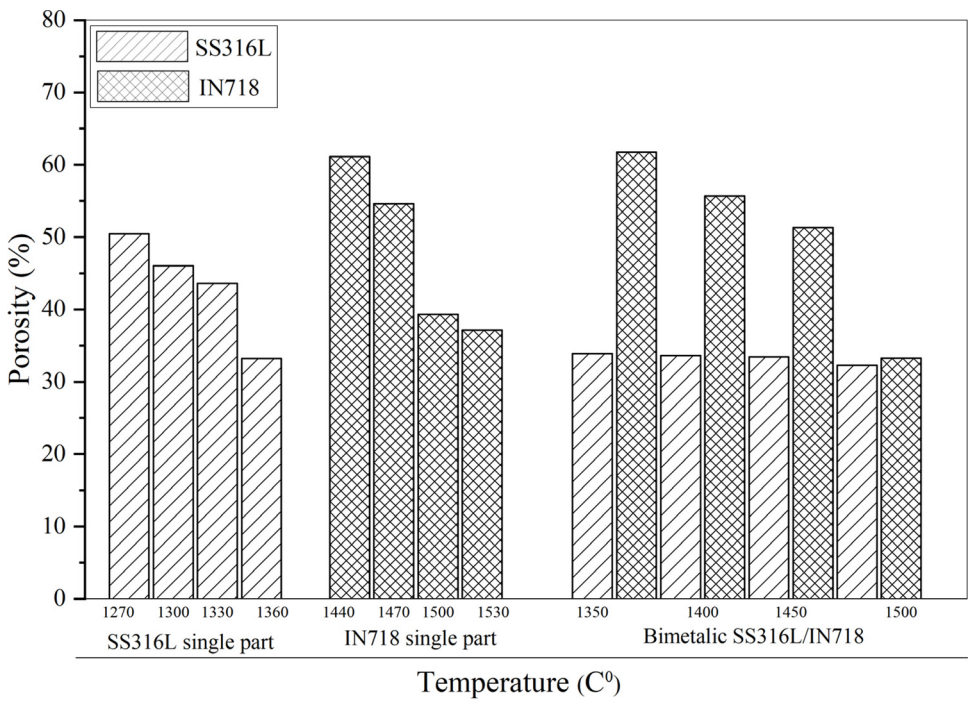

Source: Author's own work

J_ID: RPJ ART NO: 10.1108/RPJ-04-2024-0163 Date: 13-July-24 Page: 11 Total Pages: 15 4/Color Figure(s) ARTTYPE="ResearchArticle"

Figure 11 Scanning electron micrograph of sintered parts: SS316L

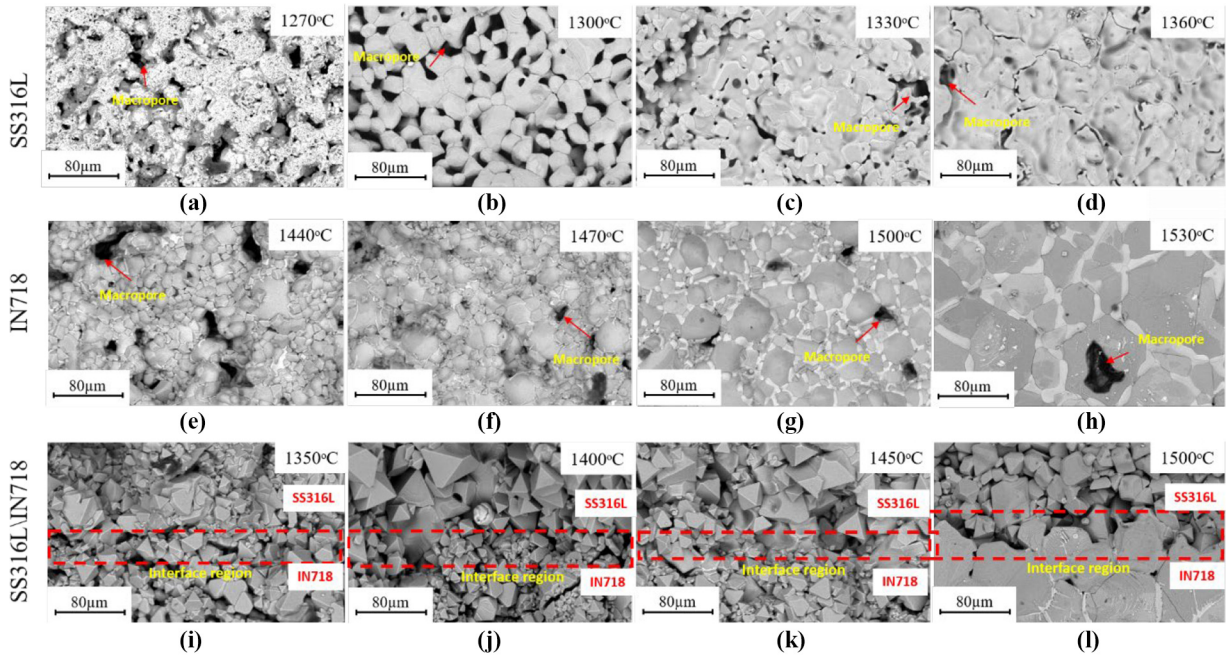

Notes: (a) 1270°C; (b) 1300°C; (c) 1330°C; (d) 1360°C, IN718; (e) 1440°C; (f) 1470°C; (g) 1500°C; (h) 1530°C, SS316L/IN718; (i) 1350°C; (j) 1400°C; (k) 1450°C; (l) 1500°C)
Source: Author's own work

accompanied by reduced porosity, aligning with similar findings in the study by Santamaria et al (Santamaria *et al.*, 2022).

The sintered IN718 parts exhibit a similar evolution of grain growth corresponding to the sintering temperature levels. Initially, small, homogeneous IN718 grains begin to fuse, forming thin grain boundaries and distributing numerous small pores in sintered parts heated at 1,440°C–1,470°C. As the temperature increases further, fine grains visibly transform into coarse grains, emphasizing the development of grain boundaries. At a temperature of 1,500°C, well-developed grains with distinct boundaries are observed, accompanied by a reduction in porosity. In the absence of adequate atmosphere control, the prolonged exposure to high heat causes both SS316L and IN718 to react with the oxygen present in the furnace environment, leading to the formation of an oxide layer that alters the melting point of pure SS316L and IN718.

The scanning electron micrograph of bimetallic materials SS316L/IN718 reveals distinct shapes in the interface region. At elevated temperatures, the morphology of SS316L interface region forms an octahedron shape and constantly has the same size on its grains in all variable temperatures. On the other hand, the interface of IN718 has remained consistent with the result of evolution morphology in IN718 single part that applying temperature under 1,500°C was not adequate to fuse grains. The interface region depicted high differences on both sides of SS316L and IN718. In an ambient atmosphere with negligible oxygen, nitrogen is present in high concentrations. Elements such as Cr, Fe and Ni are inclined to bind with oxygen during prolonged exposure to elevated temperatures. Specifically, oxygen exhibits a higher tendency to bond with Cr (Santamaria *et al.*, 2022). Consequently, oxide compounds, such as Fe_3O_4 and $FeCr_2O_4$, are identified in the XRD results.

3.5.3 *X-ray diffraction*

The three sintered samples were analyzed by X-ray diffraction to find valuable information about their crystalline structure and to identify the presence of different phases within the sintered part. Therefore, all XRD graphs will provide comprehensive information belonging to the sintered part in the detailed crystal structure, phase composition, crystallinity and correlation with the mechanical properties of those samples. The XRD pattern of the SS316L sample sintered in the environmental condition in the temperature range of 1,270°C–1,360°C (180°C increment) for 12 h is presented in [Figure 12(a)] The lower temperature has austenite phase and no ferrite phase found, but some non-metallic phases are identified such as magnetite Fe3O4, ferro chromium oxide ($FeCr_2O_4$) and chromium carbide Cr_3C_7. One of the factors that emerged as the presence of those metallic parts was driven by an uncontrolled sintering atmosphere and exposed high temperatures for a long duration. This high temperature under a normal atmosphere causes the reaction between metal and atmosphere gaseous (N_2 or O_2) resulting magnetite Fe_3O_4 and ferro chromium oxide ($FeCr_2O_4$). On the other hand, the existence of Cr_3C_7 is generated from the reaction between the carbon of burned PLA and the chromium inside the powder. Those oxidation results cause the weight gain and brittleness in the metal properties. The compounds of IN718 sintered in the environmental atmosphere at four different temperature sintering. As the

F12

J_ID: RPJ ART NO: 10.1108/RPJ-04-2024-0163 Date: 13-July-24 Page: 12 Total Pages: 15 4/Color Figure(s) ARTTYPE="ResearchArticle"

Figure 12 XRD diffractogram in the different post-processing temperature of (a) SS316L, (b) IN718 and (c) SS316L/IN718. The experimental condition under Ni/O environment

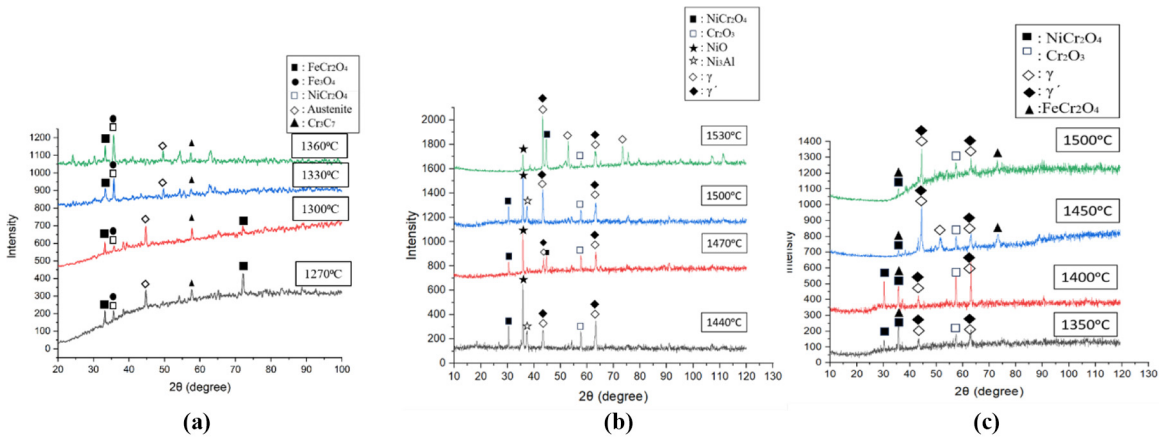

Source: Author's own work

F13 increasing temperature, it can be seen that the γ and $\gamma^{¨}$ keep stable even they reach high temperatures (1,530°C) which reflects the excellent properties of its high-temperature application. However, the phase formed by oxidation was also detected such as $NiCr_20_4$, Cr_2O_3, NiO. According to XRD results of SS316L/IN718 sintered in the various sintering temperature levels in the normal atmosphere, the dominant phase belongs to IN718 peaks which represent the γ and $\gamma^{¨}$ and its oxide. However, the peaks which belong to SS316L were only detected for ferrochromium oxide ($FeCr_2O_4$). The absence of austenite and ferrite in this bimetallic also correspond into the change of grain shape in the microstructure which the oxide compounds are more dominant.

3.5.4 Hardness

There is a significant influence correlated between hardness result and rising temperature in both materials as shown in Figure 13. Figure 13 presents that the hardness value of SS316L and IN718 sintered parts could achieve 872 HV and 755.5 HV respectively. The hardness value of SS316L and IN718 sintered parts could achieve 872 HV and 755.5 HV respectively. The related hardness result of SS316L in other research was up to 296 HV with the LDED process and possessed heat treatment. Kong *et al.* (2019) studied the mechanical properties and corrosion behavior of SS316L by SLM attained a high hardness of 280 HV. Chen *et al.* (2019) fabricated SS316L by LPBF and conducted annealing in different temperatures which can obtain the hardness value 291 HV. Meanwhile, the micro hardness of Inconel 718 fabricated by direct energy deposition has reached 289–385 HV (Li *et al.*, 2020). The bulk Inconel 718 which is processed by LMD could have 400 HV. The associated hardness values of both SS316L and IN718 in this research are considerably higher than those of previous literature hardness results. Despite the low-density

Figure 13 Vickers microhardness profile for SS316L and IN718 sintered parts in different temperature post-processinh

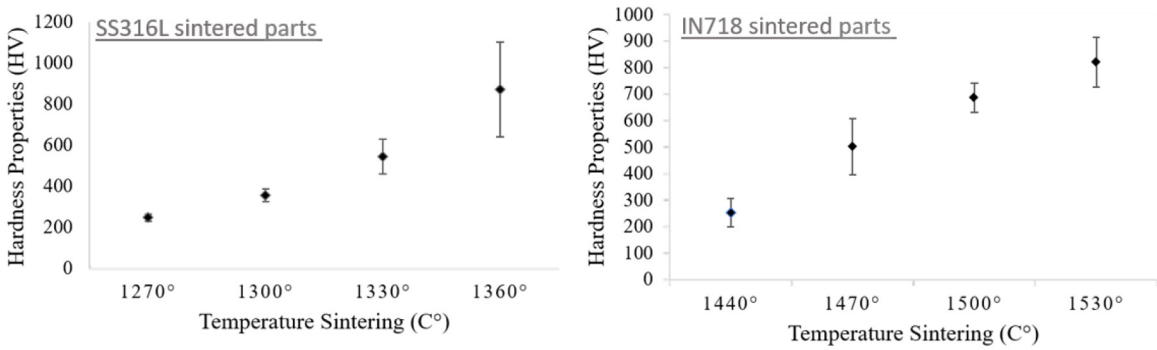

Notes: Notes: Each data point is an average of 5 independent measurements and given with standard deviation
Source: Author's own work

J_ID: RPJ ART NO: 10.1108/RPJ-04-2024-0163 Date: 13-July-24 Page: 13 Total Pages: 15 4/Color Figure(s) ARTTYPE="ResearchArticle"

percentage of SS316L and IN718, the high value of hardness is triggered by the main compound of them oxide (Sun *et al.*, 2016; Tucho *et al.*, 2018) and founded carbide (Mousapour *et al.*, 2021) which is in agreement with XRD results.

4. Conclusion

This study employed an experimental approach to fabricate metal parts from SS316L and IN718 materials using Fused Deposition Modeling (FDM), exploring the sintering process at different temperatures. The investigation extended to assess the feasibility of creating a bimetallic composite with SS316L and IN718. The study encompassed an examination of printing characteristics, thermal analysis, microstructural features and mechanical properties across three distinct sintered samples. The key findings are summarized as follows:

- The successful fabrication of SS316L, IN718 and SS316L/IN718 using the dual-nozzle FDM approach resulted in accurate dimensional printing with a tolerance of ±0.3 mm. The debinding process demonstrated a significant reduction of up to 14% in size and weight loss for all samples. Notably, while SS316L sintered results did not exhibit noticeable shrinkage, both IN718 and the combined SS316L/IN718 samples experienced a shrinkage effect.
- In the microstructure analysis, utilizing optical microscopy (OM) and scanning electron microscopy with energy-dispersive X-ray spectroscopy (SEM/EDS), it is observed that with an increase in temperature, all materials exhibit a trend toward densification and display more distinct grain boundaries. The EDS results indicate that all materials contain approximately one-fourth oxygen content, suggesting a presence of oxidation.
- Due to the longer and higher temperature exposure in the environmental atmosphere, the results of characterization in X-ray diffraction on both sides of SS316L and IN718 show the formation of some oxide layers comprising ($FeCr_2O_4$, Fe_3O_4, Cr_3C_7) for SS316L and ($NiCr_2O_4$, Cr_2O_4, NiO) for IN718 which those new phases cause the high value in the properties of hardness and brittleness.
- The mechanical testing value hardness both metals present a significant increase up to 872 HV and 755.5 HV for SS316L and IN718 which is supported by the high content of oxides.

Acknowledgements

Authors' Contribution Statement: Masrurotin, conceptualization, data curation, formal analysis, investigation, methodology; Alvian Toto Wibisono, validation, visualization, writing – original draft, writing –review and editing; Cho-Pei Jiang, conceptualization, funding acquisition, project administration, resources, software, supervision, validation, visualization, writing – original draft; Maziar Ramezani, validation, writing – original draft, supervision; Ehsan Toyserkani and Wojciech Macek, investigation, writing – review and editing.

Author Disclosure Statement: No competing financial interests exist.

Funding Statement: The authors are grateful for the financial support of the National Science and Technology Council (NSTC), Taiwan, under Grant No. 111–2221-E-027 –087 -MY2, 111–2622-E-027 –028, 112–2218-E-A49 –028, NTUT-Gdańsk Join Research Program (NTUT-Gdańsk Tech-113–02) and Gdańsk University of Technology, 1/1/2023/IDUB/II.1a/Au+ grant number under the Aurum plus — Excellence Initiative—Research University.

References

Abdulhameed, O., Al-Ahmari, A., Ameen, W. and Mian, S.H. (2019), "Additive manufacturing: challenges, trends, and applications", *Advances in Mechanical Engineering*, Vol. 11 No. 2, p. 1687814018822880.

Balbaa, M., Mekhiel, S., Elbestawi, M. and Mcisaac, J. (2020), "On selective laser melting of inconel 718: densification, surface roughness, and residual stresses", *Materials & Design*, Vol. 193, p. 108818.

Bandyopadhyay, A., Zhang, Y. and Onuike, B. (2022), "Additive manufacturing of bimetallic structures", *Virtual and Physical Prototyping*, Vol. 17 No. 2, pp. 256-294.

Boschetto, A., Bottini, L., Miani, F. and Veniali, F. (2022), "Roughness investigation of steel 316L parts fabricated by metal fused filament fabrication", *Journal of Manufacturing Processes*, Vol. 81, pp. 261-280.

Caminero, M.Á., Romero, A., Chacón, J.M., Núñez, P.J., García-Plaza, E. and Rodríguez, G.P. (2021), "Additive manufacturing of 316L stainless-steel structures using fused filament fabrication technology: mechanical and geometric properties", *Rapid Prototyping Journal*, Vol. 27 No. 3, pp. 583-591.

Chen, N., Ma, G., Zhu, W., Godfrey, A., Shen, Z., Wu, G. and Huang, X. (2019), "Enhancement of an additive-manufactured austenitic stainless steel by post-manufacture heat-treatment", *Materials Science and Engineering: A*, Vol. 759, pp. 65-69.

Jiang, C.-P., Wibisono, A.T. and Pasang, T. (2021), "Selective laser melting of stainless steel 316l with face-centered-cubic-based lattice structures to produce rib implants", *Materials*, Vol. 14 No. 20, p. 5962.

Jiang, C.-P., Wibisono, A.T., Wang, S.-H., Pasang, T. and Ramezani, M. (2022), "Selective laser melting of free-assembled stainless steel 316L hinges: optimization of volumetric laser energy density and joint clearance", *Metals*, Vol. 12 No. 7, p. 1223.

Jiang, D. and Ning, F. (2021), "Additive manufacturing of 316L stainless steel by a printing-debinding-sintering method: effects of microstructure on fatigue property", *Journal of Manufacturing Science and Engineering*, Vol. 143 No. 9, p. 91007.

Jongprateep, O., Jitanukul, N., Saphongxay, K., Petchareanmongkol, B., Bansiddhi, A., Laobuthee, A., Lertworasirikul, A. and Techapiesancharoenkij, R. (2022), "Hydroxyapatite coating on an aluminum/bioplastic scaffold for bone tissue engineering", *RSC Advances*, Vol. 12 No. 41, pp. 26789-26799.

Kan, X., Yang, D., Zhao, Z. and Sun, J. (2021), "316L FFF binder development and debinding optimization", *Materials Research Express*, Vol. 8 No. 11, p. 116515.

Kong, D., Dong, C., Ni, X., Zhang, L., Yao, J., Man, C., Cheng, X., Xiao, K. and Li, X. (2019), "Mechanical properties and corrosion behavior of selective laser melted

J_ID: RPJ ART NO: 10.1108/RPJ-04-2024-0163 Date: 13-July-24 Page: 14 Total Pages: 15 4/Color Figure(s) ARTTYPE="ResearchArticle"

316L stainless steel after different heat treatment processes", *Journal of Materials Science & Technology*, Vol. 35 No. 7, pp. 1499-1507.

Kurose, T., Abe, Y., Santos, M.V., Kanaya, Y., Ishigami, A., Tanaka, S. and Ito, H. (2020), "Influence of the layer directions on the properties of 316l stainless steel parts fabricated through fused deposition of metals", *Materials*, Vol. 13 No. 11, p. 2493.

Li, Z., Chen, J., Sui, S., Zhong, C., Lu, X. and Lin, X. (2020), "The microstructure evolution and tensile properties of inconel 718 fabricated by high-deposition-rate laser directed energy deposition", *Additive Manufacturing*, Vol. 31, p. 100941.

Liu, B., Wang, Y., Lin, Z. and Zhang, T. (2020), "Creating metal parts by fused deposition modeling and sintering", *Materials Letters*, Vol. 263, p. 127252.

Mahmud, A., Ayers, N., Huynh, T. and Sohn, Y. (2023), "Additive manufacturing of SS316L/IN718 bimetallic structure via laser powder bed fusion", *Materials*, Vol. 16 No. 19, p. 6527.

Maksimkin, I.P., Yukhimchuk, A.A., Malkov, I.L., Boitsov, I. E., Musyaev, R.K., Buchirin, A.V., Baluev, V.V., Vertei, A. V., Shevnin, E.V. and Shotin, S.V. (2022), "Effect of hydrogen on the structure and mechanical properties of 316L steel and Inconel 718 alloy processed by selective laser melting", *Materials*, Vol. 15 No. 14, p. 4806.

Mousapour, M., Salmi, M., Klemettinen, L. and Partanen, J. (2021), "Feasibility study of producing multi-metal parts by fused filament fabrication (FFF) technique", *Journal of Manufacturing Processes*, Vol. 67, pp. 438-446.

Pang, J.H.L., Kaminski, J. and Pepin, H. (2019), "Characterisation of porosity, density, and microstructure of directed energy deposited stainless steel AISI 316L", *Additive Manufacturing*, Vol. 25, pp. 286-296.

Santamaria, R., Salasi, M., Bakhtiari, S., Leadbeater, G., Iannuzzi, M. and Quadir, M.Z. (2022), "Microstructure and mechanical behaviour of 316L stainless steel produced using sinter-based extrusion additive manufacturing", *Journal of Materials Science*, Vol. 57 No. 21, pp. 1-17.

Shi, W., Wang, P., Liu, Y., Hou, Y. and Han, G. (2020), "Properties of 316L formed by a 400 W power laser selective laser melting with 250 μm layer thickness", *Powder Technology*, Vol. 360, pp. 151-164.

Singh, S.P., Aggarwal, A., Upadhyay, R.K. and Kumar, A. (2021), "Processing of IN718-SS316L bimetallic-structure using laser powder bed fusion technique", *Materials and Manufacturing Processes*, Vol. 36 No. 9, pp. 1028-1039.

Sun, Z., Tan, X., Tor, S.B. and Yeong, W.Y. (2016), "Selective laser melting of stainless steel 316L with low porosity and high build rates", *Materials & Design*, Vol. 104, pp. 197-204.

Thompson, Y., Gonzalez-Gutierrez, J., Kukla, C. and Felfer, P. (2019), "Fused filament fabrication, debinding and sintering as a low cost additive manufacturing method of 316L stainless steel", *Additive Manufacturing*, Vol. 30, p. 100861.

Tucho, W.M., Lysne, V.H., Austbø, H., Sjolyst-Kverneland, A. and Hansen, V. (2018), "Investigation of effects of process parameters on microstructure and hardness of SLM manufactured SS316L", *Journal of Alloys and Compounds*, Vol. 740, pp. 910-925.

Wei, X., Behm, I., Winkler, T., Scharf, S., Li, X. and Bähr, R. (2022), "Experimental study on metal parts under variable 3D printing and sintering orientations using bronze/PLA hybrid filament coupled with fused filament fabrication", *Materials*, Vol. 15 No. 15, p. 5333.

Yakout, M., Elbestawi, M. and Veldhuis, S.C. (2018), "A study of thermal expansion coefficients and microstructure during selective laser melting of invar 36 and stainless steel 316L", *Additive Manufacturing*, Vol. 24, pp. 405-418.

Yang, S.W., Yoon, J., Lee, H. and Shim, D.S. (2022), "Defect of functionally graded material of inconel 718 and STS 316L fabricated by directed energy deposition and its effect on mechanical properties", *Journal of Materials Research and Technology*, Vol. 17, pp. 478-497.

You, S., Jiang, D., Wang, F. and Ning, F. (2023), "Anisotropic sintering shrinkage behavior of stainless steel fabricated by extrusion-based metal additive manufacturing", *Journal of Manufacturing Processes*, Vol. 101, pp. 1508-1520.

Corresponding author

Cho-Pei Jiang can be contacted at: jcp@ntut.edu.tw